Ahuir-Torres, JI, Evans, S, Opoz, TT, Bashir, M and Kotadia, HR

Enhanced Durability of MoS2-Coated C2800 brass Achieved via Combined Laser-Induced Texture Patterns with Various Morphologies

Enhanced Durability of MoS_2-Coated C2800 brass Achieved via Combined Laser-Induced Texture Patterns with Various Morphologies

J.I. Ahuir-Torres, S. Evans, T.T. Öpöz, M. Bashir, H.R. Kotadia

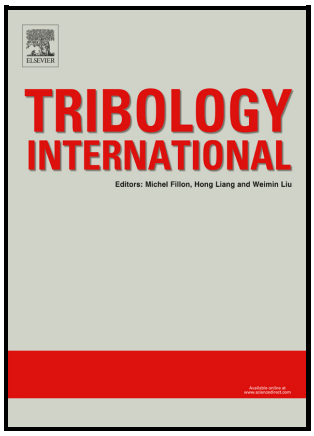

PII: S0301-679X(25)00798-4

DOI: https://doi.org/10.1016/j.triboint.2025.111303

Reference: JTRI111303

To appear in: *Tribology International*

Received date: 11 August 2025
Revised date: 6 October 2025
Accepted date: 9 October 2025

Please cite this article as: J.I. Ahuir-Torres, S. Evans, T.T. Öpöz, M. Bashir and H.R. Kotadia, Enhanced Durability of MoS_2-Coated C2800 brass Achieved via Combined Laser-Induced Texture Patterns with Various Morphologies, *Tribology International,* (2025) doi:https://doi.org/10.1016/j.triboint.2025.111303

Enhanced Durability of MoS_2-Coated C2800 brass Achieved via Combined Laser-Induced Texture Patterns with Various Morphologies

J.I. Ahuir-Torres[1], S. Evans[1], T.T. Öpöz[1], M. Bashir[2] and H. R. Kotadia[1]

[1]School of Engineering, Liverpool John Moores University, Liverpool, L3 3AF, UK.

[2]Civil and Environmental Engineering, University of Liverpool, Liverpool, L69 7ZX, UK

*Corresponding Author´s email: j.i.ahuirtorres@ljmu.ac.uk

Abstract:
Cu–Zn (C28000) brass is widely used in friction-intensive applications but has low wear resistance, often requiring continuous lubrication. Molybdenum disulphide (MoS_2) is an effective solid lubricant; however, its performance declines over time due to depletion. Laser surface texturing (LST) can extend lubricant retention, with texture characteristics being critical. While individual parameters such as texture size and orientation have been studied, the combined effect of texture shape, hybrid pattern configurations, and texture density (TD) on lubricant replenishment intervals remains underexplored. This work systematically investigates single-shape and combined-shape texture patterns with varying TD on C28000 brass under MoS_2 lubrication. Patterns were produced using a fibre infrared nanosecond pulsed laser and tested via ball-on-disc experiments. Samples were examined using optical profilometry, scanning electron microscopy, and energy-dispersive spectroscopy. Increasing TD from 5% to 75% extended the MoS_2 retention period by at least 65% for all texture designs. Less common morphologies, such as concentric rings and dimple–grid patterns, were also examined and further assessed using finite element simulations. Concentric ring textures at the highest TD achieved the longest retention (28 times longer compared to non-TD samples) due to their closed-loop geometry, which promoted lubricant entrapment and delayed depletion. Grid textures showed the shortest retention because open channels facilitated rapid lubricant escape. Hybrid patterns offered no benefit and sometimes reduced performance by disrupting reservoir continuity. These results quantify how texture geometry and TD influence lubricant depletion through changes in reservoir continuity and escape pathways, providing design guidelines for extending service intervals of solid-lubricated brass components.

Keywords: Laser surface texturing; Texture shape and density; Molybdenum disulphide; Brass; Lubrication service life.

1. Introduction

Cu–Zn alloys, commonly known as brass, are extensively used in industrial components such as pistons, gears, and bushings due to their combination of friction resistance, formability, corrosion resistance, and high mechanical strength [1-4]. Despite these advantages, their relatively low hardness makes them susceptible to abrasive and adhesive wear, potentially reducing component lifespan and necessitating surface protection strategies [1, 3].

To overcome these wear-related challenges, surface engineering strategies such as lubrication and surface texturing are increasingly adopted. Lubrication, in particular, plays a central role in minimising wear and friction. Among the different types: liquid, semi-solid, and solid-solid lubricants are especially advantageous under high-temperature or chemically aggressive environments. Molybdenum disulfide (MoS_2) stands out as a widely used solid lubricant due to its excellent thermal stability, chemical inertness, and low coefficient of friction (COF) [5, 6]. However, the need for periodic reapplication limits its long-term efficiency and increases operational costs. This underscores the need for integrated solutions, such as surface texturing techniques, that not only improve the retention and effectiveness of solid lubricants but also enhance the intrinsic wear resistance of brass surfaces, thus forming the motivation for the present investigation.

Surface texturing is a promising technique for enhancing the effectiveness of solid lubricants by providing micro-reservoirs for lubricant retention, reducing real contact area, and promoting debris entrapment, thereby improving tribological performance under severe conditions. Various approaches have been explored for surface texturing, including mechanical methods [7], chemical etching [8], ion beam irradiation [9], laser [10, 11], electrochemical machining [12], and electrical discharge machining (EDM) [13]. However, among these, laser surface texturing (LST) has gained prominence due to its distinct advantages: high reproducibility, eco-friendly operation, non-contact processing, and precise control over texture geometry and distribution [10, 11, 14]. These attributes not only enable the fine-tuning of surface properties but also allow seamless integration with automated manufacturing systems, making LST a particularly attractive method for improving the wear resistance and lubrication efficiency of brass components.

Despite extensive investigations on MoS_2-coated dimple textures, most studies have been conducted on hard substrates such as GCr15 steel [15] [16], 9Cr18 stainless steel [17], Ti6Al4V [18-20], and Al-Si alloys [21], where the substrate offers high resistance to thermal deformation and plastic flow during laser processing and sliding. In contrast, Cu-Zn alloys like brass, despite their widespread industrial usage in tribologically demanding components, have received comparatively little attention. Their relatively low hardness makes them more vulnerable to laser-induced thermal effects, such as recast layers or microstructural softening, which may alter the efficacy of both the texture and the lubricant. Moreover, the performance of MoS_2 coatings on laser-dimpled brass surfaces under varying texture densities (TD) remains underexplored. Given that increased TD has been shown to extend MoS_2 lubricant life and lower the coefficient of friction (COF) in hard substrates [20–22, 24–26], it is critical to assess whether similar benefits can be replicated in softer metals. Thus, this study aims to evaluate the tribological behaviour of laser-dimpled brass surfaces coated with MoS_2, focusing on how varying TD influences COF, wear rate, and surface integrity under dry sliding conditions. This investigation helps bridge the knowledge gap in non-ferrous alloy applications and supports the development of durable, self-lubricating brass components.

Among texture parameters, TD plays a crucial role in determining tribological behaviour. Numerous studies on MoS_2-coated dimples have shown that increasing TD extends lubricant service life and reduces the coefficient of friction (COF) under suitable conditions [15] [16] [17] [18-20] [21] [24] [25] [26]. An increase in the TD of the dimple pattern contributes to the extension of the lubricant service life [19-21, 24-26], regardless of material, texture shape and dimensions. The incorporation of dimple patterns has also been observed to reduce the COF of the MoS_2 coating; however, this reduction depends on TD and specific tribological conditions. Feng et al. [17] reported that an increase in TD led to a decrease in COF of the MoS_2-Ti coating deposited via sputtering on 9Cr18 stainless steel. Li et al. [23] observed that an increase in the temperature resulted in a higher COF due to the MoO_3 formation. Similarly, Hu et al [21] investigated the TD effect on COF of the MoS_2 coating applied to Al-Si alloy under various loads and sliding speeds. They reported that high TD reduced COF under high load/speed, but increased it under low-load, low-speed conditions. Hua et al. [16] examined the influence of dimple pattern TD on MoS_2 coating using rolling ball-on-disc testing under various conditions. They found that dimple patterns with TD values of 9% and 19% exhibited the lowest COF. This phenomenon is attributed to low TD hindering MoS_2 coating formation, while excessive TD increases surface roughness. Xia et al. [15] observed similar behaviour for a MoS_2 coated dimple pattern on GCr15 steel. Hu et al. [24] studied the influence of TD on COF of burnished and hot-pressure-deposited MoS_2 coatings. Their study demonstrated that increasing TD reduced the COF of burnished MoS_2 coatings, while COF remained unchanged for hot-pressure-deposited MoS_2 coatings.

Other types of texture patterns have also been evaluated in previous investigations reported in the literature. Zhang et al. [27] investigated the influence of groove patterns on the tribological behaviour of MoS_2 coating applied to TiAlN substrates. Similar to dimple patterns, groove pattern exhibited extended lubricant service life compared to non-textured samples. Xing et al. [28] observed a similar trend for MoS_2 coated groove patterns on Al_2O_3 / TiC ceramic. Xing et al. [29] investigated the effect of the groove shape, specifically straight-line and wave morphologies, on tribological properties of the MoS_2 coated Si_3N_4 / TiC ceramic. Their findings indicated that the wave-shaped grooves exhibited greater friction and wear resistance than the other samples. Bagade et al. [30] assessed the tribological properties of grid and ellipsoid patterns under MoS_2 lubrication. Their study concluded that the ellipsoidal geometry offered optimal wear and friction resistance due to an enhanced interlocking effect within the MoS_2 coating. Arenas et al. [20] analysed the impact of TD on the tribological properties of MoS_2-coated rhombus-like patterns. Their results indicated that increasing TD extended lubricant service life across all patterns. Notably, the rhombus-like patterns exhibited anisotropic lubricant retention, with the short diagonal orientation yielding the longest service time. The angle of the rhombus patterns also exhibited a significant effect on tribological properties, with 45^o identified as the optimal angle.

Previous studies investigating combined texture patterns on the tribological behaviour of MoS_2 coatings remain scarce. Segu et al. [31] examined the combination of circular patterns with triangular or square elements on MoS_2-coated 52100 steel and reported that increasing TD improved the coating's tribological performance. Among their findings, circular–triangular combinations exhibited the best performance, attributed to more efficient lubricant ejection from the textured cavities. Despite these insights, the broader effects of hybrid texture configurations and alternative geometries such as grid and concentric ring patterns have not been systematically explored. Moreover, while LST has been extensively studied on hard substrates, limited attention has been given to understanding how similar approaches perform

on softer metals where thermal and plastic deformation effects can strongly influence surface integrity and lubrication efficiency.

In this study, the tribological performance of MoS_2-coated C28000 brass surfaces was systematically investigated using laser-generated single and multi-type textures. The texture types included dimples, grooves, grids, and concentric rings, as well as their hybrid combinations (dimple–grid, grid–dimple, concentric ring–grid, and grid–concentric ring), with TD varied between 5% and 75%. Surface texturing was achieved using a nanosecond pulsed fibre infrared laser, and the samples were evaluated through ball-on-disc tribological tests to assess friction and wear behaviour. To further elucidate the mechanisms of lubricant retention and ejection in complex textures, finite element analysis (FEA) simulations were conducted using ANSYS software. This combined experimental–computational framework provides a comprehensive understanding of how texture geometry and density, particularly in unconventional and hybrid configurations, influence the tribological performance of MoS_2-coated brass, offering valuable insights for designing durable, self-lubricating components in engineering applications.

2. Materials and methods

2.1. Material

The test specimens were prepared from commercially available C28000 brass (Cu–37Zn) supplied by Allied Copper Alloy Ltd. The chemical composition of the alloy is presented in **Table 1**. Each specimen had dimensions of 30 × 30 × 3 mm.

Table 1. Chemical composition of C28000 brass (wt.%).

Element	Cu	Zn	Ni	Fe	Pb	Sn	Al
Concentration (wt.%)	62.35	37.00	0.30	0.10	0.10	0.10	0.05

Samples were polished to a surface roughness (Sa) of 100 nm using P1200 grit SiC abrasive paper (supplied by Struers), which is considered the optimal surface roughness for laser processing [32]. Prior to LST and tribological testing, the samples were cleaned using the following procedure: detergent wash, freshwater rinse, distilled water soaking, isopropanol spray, and heat drying. All cleaning materials and equipment were supplied by RS Components Ltd.

2.2. Laser system

LST was performed using a laser setup (**Fig. 1**) consisting of an infrared (IR) nanosecond pulsed fibre laser (SPI Laser G3 20W), coupled with a 1064 nm beam expander (Linos (Qioptiq) 2-8x), a scanning galvanometer (Nutfield Extreme-15-YAG) controlled by SAMLight v3.05 software (SCAPS Gmbh), and a 100 mm focal length f-theta lens (Linos Ronar F-Theta focal lens). A three-axis automated table (Aerotech Limited, UK) was used to hold and move the samples.

The laser can operate at a wavelength of 1064 ± 5 nm in transverse electromagnetic mode was 00, with a beam quality (M^2) of 2.1. It offers pulse durations from 9 ns to 200 ns, and repetition frequencies ranging from 1 kHz to 500 kHz. The maximum average power is 20 W, with a peak pulse energy of 800 µJ. The beam expander produces a raw beam diameter of 5.7 mm. The galvanometer enables beam scanning at speeds from 10^{-2} mm/s to $2x10^4$ mm/s. Although

the brass alloys exhibit only moderate absorption to infrared radiation, 1064 nm fibre lasers are widely employed across multiple sectors because of their operational versatility and high pulse energy.

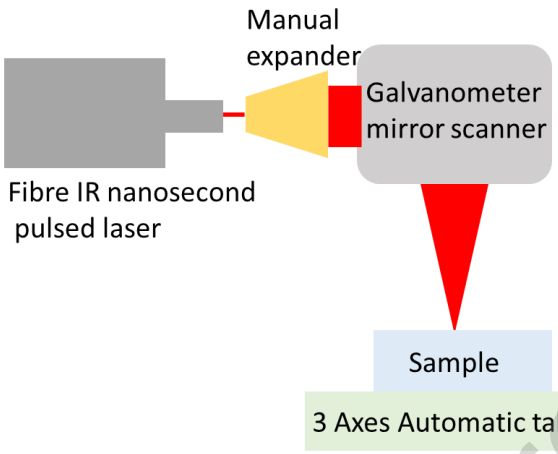

Fig. 1. Schematic drawing of the laser equipment setup.

2.3. Laser surface texturing

The surface patterns were produced using either a single texture type or a combination of two different texture types. The individual texture types included dimples, grooves, grids, and concentric rings. The laser parameters for each pattern are detailed in **Table 2**. Notably, these laser parameters were selected to produce the textures with the width-to-depth aspect ratio of 0.1, which previous studies have identified as the optimal [22, 33, 34]. The topographical features of the textures are described in detail in Section 3.1.

Table 2. Laser processing parameters for individual texture.

Parameter	Value
Pulse length (ns)	200
Focused laser beam diameter (μm)	51
Pulse number for dimple	1
Scan rate for groove and ring (mm/s)	400
Pulse repetition frequency (kHz)	25
Atmosphere	Air
Pulse energy for dimple (μJ)	670
Pulse energy for groove and ring (μJ)	233

Eight texture patterns were designed (**Fig. 2**) and categorised into single- and multi-texture types. The single-texture patterns included dimples, grooves, grids, and concentric rings (**Fig. 2(a–d)**). For the dimple pattern (**Fig. 2(a)**), the horizontal and vertical inter-dimple spacing were comparable. In the grid pattern (**Fig. 2(c)**), horizontal and vertical grooves were spaced at equal intervals. The concentric ring pattern (**Fig. 2(d)**) consisted of one or more rings with a central dimple, with vertical and horizontal distances between central dimples kept constant. All inter-feature distances decreased as texture density increased. The multi-texture patterns were designed by combining single textures in different configurations: (1) Dimples-grid (**Fig. 2(e)**): Dimples were embedded within grid squares. The horizontal spacing between dimples and the overall grid area remained constant, while the number of dimple lines per grid increased with texture density, reducing the vertical distance between adjacent dimples. (2) Grids-dimple (**Fig. 2(f)**): Similar to dimples-grid, but with a single dimple cantered in each square. The

square area decreased as texture density increased. (3) Concentric rings-grid (**Fig. 2(g)**): Concentric rings were placed inside each grid square. The overall grid area remained constant, while the number of rings increased with texture density. (4) Grids-concentric ring (**Fig. 2(h)**): A single ring was placed at the centre of each grid square, with the square area decreasing as texture density increased. This design approach allowed controlled variation of texture type, density, and feature arrangement, facilitating systematic evaluation of tribological performance.

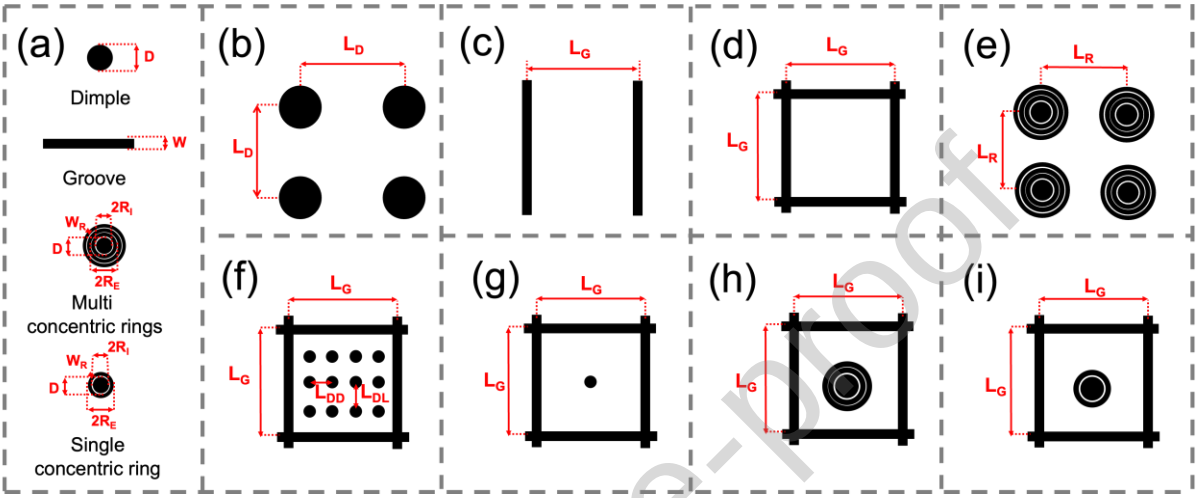

Fig. 2. Schematic illustrations of the surface textures: (a) individual texture, (b) dimple, (c) groove, (d) grid, (e) concentric ring, (f) dimples-grid, (g) grid-dimple, (h) concentric ring-grid, and (i) grid-concentric ring pattern.

The patterns were designed with texture density (TD) of 5%, 25%, 50%, and 75%. TD was calculated using Eq. (1)-(8), corresponding to the dimple, groove, grid, concentric ring, dimples-grid, grids-dimple, concentric rings-grid and, grids-concentric ring patterns, respectively.

$$TD = 100\frac{\pi D^2}{4L_D^2} \quad \text{(Dimple pattern) (1)}$$

$$TD = 100\frac{W}{L_G} \quad \text{(Groove pattern) (2)}$$

$$TD = 100\frac{2WL_G - W^2}{L_G^2} \quad \text{(Grid pattern) (3)}$$

$$TD = 100\frac{\pi[\frac{D^2}{4} + \sum_1^N (R_{E,i}^2 - R_{I,i}^2)]}{L_R^2} \quad \text{(Concentric ring pattern) (4)}$$

$$TD = 100(\frac{2WL_G - W^2}{L_G^2} + \frac{\pi D^2}{4L_{DD}L_{DL}}) \quad \text{(Dimples-grid pattern) (5)}$$

$$TD = 100(\frac{2WL_G - W^2}{L_G^2} + \frac{\pi D^2}{4L_G^2}) \quad \text{(Grids-dimple pattern) (6)}$$

$$TD = 100\frac{2WL_G - W^2 + \pi[\sum_1^N (R_{E,i}^2 - R_{I,i}^2)]}{L_G^2} \quad \text{(Concentric rings-grid pattern) (7)}$$

$$TD = 100\frac{2WL_G - W^2 + \pi[(R_E^2 - R_I^2)]}{L_G^2} \quad \text{(Grid-Concentric ring pattern) (8)}$$

Where, D is the dimple diameter, L_D is distance between dimples, W is the groove width, L_G is the distance between grooves, R_E is the external radius of the ring, R_I is the internal radius of the ring, L_{DD} is the distance between dimples in the same line, and L_{DL} is the distance between dimple lines.

2.4 Tribological tests

Tribological testing was carried out using a pin-on-disc tester (Koehler K93590) with a ball-on-disc configuration under ambient conditions. The disc was the sample, and the counter-body was SAE52100 steel ball, supplied by Bearing Warehouse. The ball-on-disc testing conditions are summarised in **Table 3**.

Table 3. Ball-on-disc testing parameters.

Parameter	Value
Rotational speed (rpm)	100.0
Linear velocity (mm/s)	100.0
Worn track radius (mm)	10.0
Load (N)	10.0
Ball radius (mm)	6.0
*Semi contact width (μm)	60.0
*Effective contact radius (mm)	1.5
*Indentation (μm)	1.4
*Mean contact pressure (MPa)	760.0
*Maximum contact pressure (MPa)	1130.0
Atmosphere	Natural air
Temperature (K)	23
Humidity (%)	80

*Values calculated using https://www.tribology-abc.com/calculators/e2_1.htm

Most of the tests were conducted under solid lubricant (MoS_2) conditions. Only non-textured samples were subjected to dry testing for 300 seconds, serving as a baseline. The samples were coated with MoS_2 using an aerosol spray with 70% in volume of MoS_2 purity (CRC Industrial Products "Dry Moly Lube" from RS Components). The MoS_2 coating was cured for 24 hours post-spraying, achieving a thickness of 15 ± 3 μm, measured by optical light profilometry (as detailed in section 2.5). The tests with and without MoS_2 on the non-textured sample were used as references. To ensure the reliability and validity of the results, each test was performed a minimum of three times.

2.5. Characterisation and analysis

The topography and morphology of the texture patterns were characterised using an optical profiler (Bruker ContourGT). Measurements were conducted using the vertical scanning interferometry (VSI) method with green light and a 50x magnification objective, operated 1.0 numerical aperture. Single texture characteristics, including diameter, width, and depth, were determined by averaging measurements from ten randomly selected textured samples.

The surface morphology and elemental composition of the samples were analysed using a Hitachi TM4000 Plus Tabletop scanning electron microscope (SEM). Imaging was performed using both secondary electron (SE) and backscattered electron (BSE) detectors, operating at an accelerating voltage of 15 kV, a current of 70 µA, and a spot size of 2 µm. Chemical composition analysis was carried out using energy dispersive spectroscopy (EDS), employing BSE detection with the same accelerating voltage and current, but with a 3 µm spot size.

2.6. Finite element analysis simulations

The simulations of the finite element analysis were conducted to evaluate the influence of the hybrid texture pattern in the normal stress across the surface. The normal stress on textured surfaces is a key factor in determining the ejection rate of the solid lubricant, which defines the lubrication service life [35]. The simulations were only focused on the dimple, grid, concentric ring, dimples-grid, grids-dimple, concentric rings-grid, and grids-concentric ring patterns. Notably, groove patterns were excluded from the simulations, as their normal stress has already been extensively examined in previous studies [35-39]. Hybrid patterns incorporating grooves was not considered in this study. A TD of 50% was selected for designing the simulated texture patterns because of this value lies near midpoint of TD range employed in the experimental analyses.

All simulation systems formed of with two-body configuration, consisting of the ball (counter-body) and samples (**Fig. 3**). The ball, composed of SAE52100 steel, had a diameter of 6.0 mm, while the samples, made of C28000, measured 1.0 mm x 1.0 mm with a thickness of 0.8 mm. The texture patterns were designed based on the experimental parameters of diameter, width, spacing between textures, and depth (Section 3.1.). The centre of each sample was placed at coordinate origin across all simulations. The ball centre was localised at origin of the Y axis, -0.45 mm along the X axis, and 3.8 mm (0.8 mm corresponding to thickness of the sample) along the Z axis. The contact area was between the textured surface and the ball and was dynamically adjusted according to the ball displacement. The coefficient of friction was fixed at 0.15 in alignment to the experimental results (Section 3.2). A normal force of -10 N was applied to the ball, which was displaced at X-axis with a velocity of 100 mms^{-1}. The displacement was applied solely to the ball to prevent additional stresses arising in the sample from the movement. Samples were constrained to avoid their displacement with the ball movement. Gravity force was incorporated in all simulations with a magnitude of 9.807 NKg^{-1}. A triangular mesh with 0.01 mm of size was employed in the simulations, which was smaller than the characteristic surface dimensions of the textures (≈ 45 µm, Section 3.1). The bounder conditions were equal to the size of the samples and ball.

The assumptions used in the simulations are summarised below.

- The dimensions of the simulated samples (1.0 mm x 1.0 mm x 0.8 mm) were reduced in comparison with the experimental specimens (30 mm x 30 mm x 3 mm), as the width contact of the ball with the surface was limited 120 µm (**Table 3**)
- The deformations of the samples and the ball were neglected because of MoS_2 lubricant provides effective protection against wear.

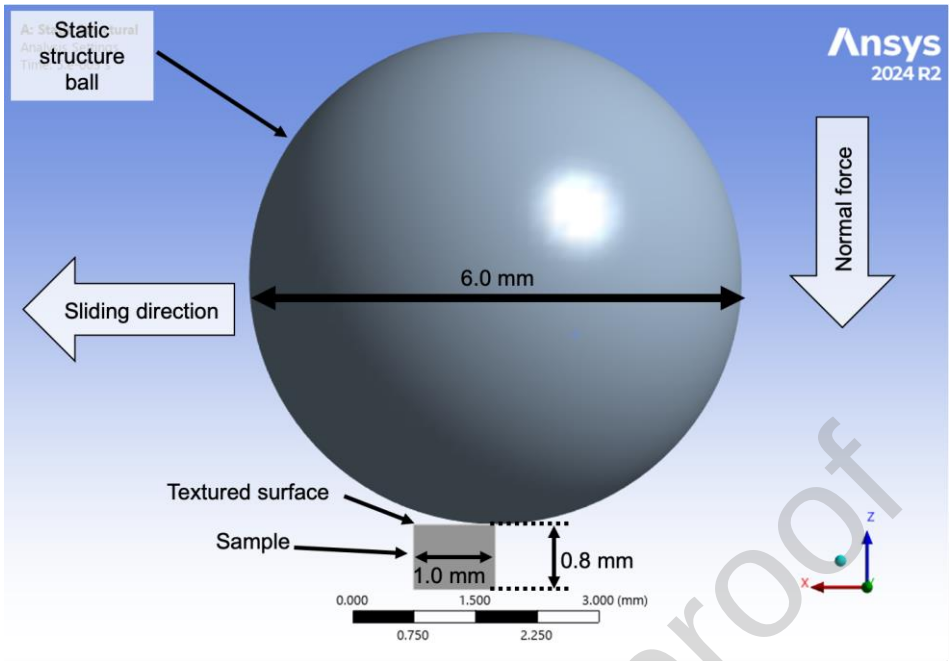

Fig. 3. Finite element analysis (FEA) simulation setup.

3. Results and discussion

3.1. Texture Analysis: Morphological and Geometrical Characterisation

All individual texture patterns (**Fig. 4**) displayed a spherical cap-like topography, consistent with the typical U-type texture morphology reported in the literature [40, 41]. This morphology arises because only the peak region of the Gaussian laser beam provides sufficient energy fluence to effectively ablate the material [17]. Particularly, each texture exhibited a pronounced crest along its edges, attributed to rapid cooling and the displacement of molten material during laser processing.

The accumulation of molten material at the periphery of the laser-affected zone results from the combined effects of recoil pressure, hydrodynamic expansion, and phase explosion mechanisms. As the laser irradiates the surface, vaporised material exerts pressure on the molten pool, driving it outward toward cooler regions [23, 42]. Additionally, thermal gradients induce material migration from the high-temperature centre toward the cooler edges, in accordance with the second law of thermodynamics [43]. The phase explosion mechanism, characterised by the formation and collapse of liquid-gas bubbles, further contributes to edge crest formation by forcibly redistributing molten material upon gas bubble rupture [42-44].

Spherical particles observed beyond the laser-affected zones are similarly attributed to the phase explosion effect. These particles result from the ejection of molten droplets during bubble collapse, which subsequently solidify rapidly upon deposition [42, 43].

Quantitative measurements of the dimple (**Fig. 4(a)**), groove (**Fig. 4(b)**), and ring (**Fig. 4(c)**) textures revealed average diameters and widths of 45 ± 4 μm and 42 ± 4 μm, respectively, with depths of approximately 4.5 ± 0.4 μm. These dimensions correspond to a depth-to-diameter (or width) aspect ratio of ~0.1, aligning well with optimal ratios reported in prior studies for tribological performance enhancement [22, 33].

Furthermore, the overall arrangement of these patterns, as a function of TD, is shown in **Fig. 5** and summarized in **Table 4**. For the more complex concentric ring patterns, the consistent spacing of 45 μm between rings demonstrates a high degree of process control. This value is identical to the distance between the single dimple and ring textures, indicating a scalable and repeatable fabrication process. The geometry of these complex patterns is further defined by the R_E and R_I, providing a precise framework for understanding their macroscopic morphology.

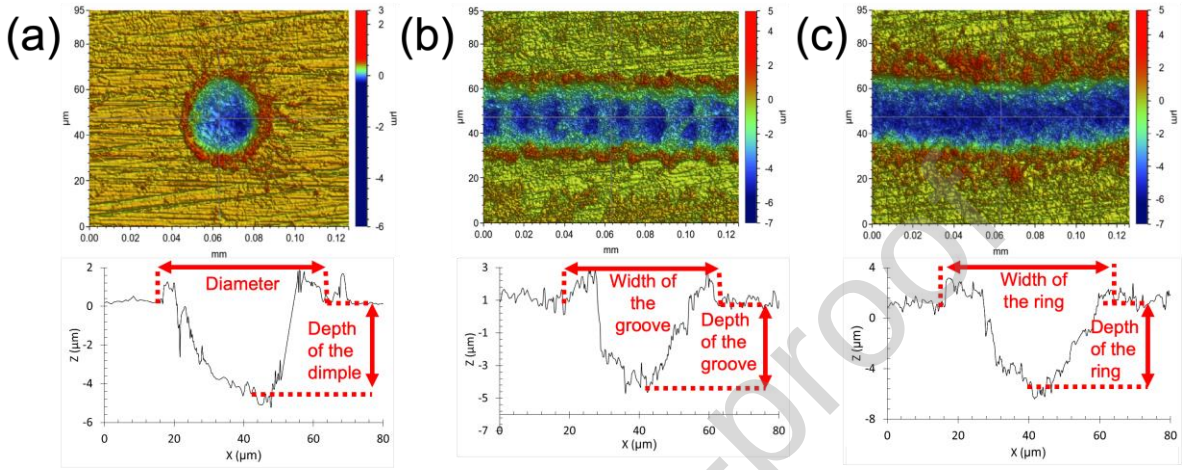

Fig. 4. Image and profile of the single texture, (a) dimple, (b) groove, and (c) ring.

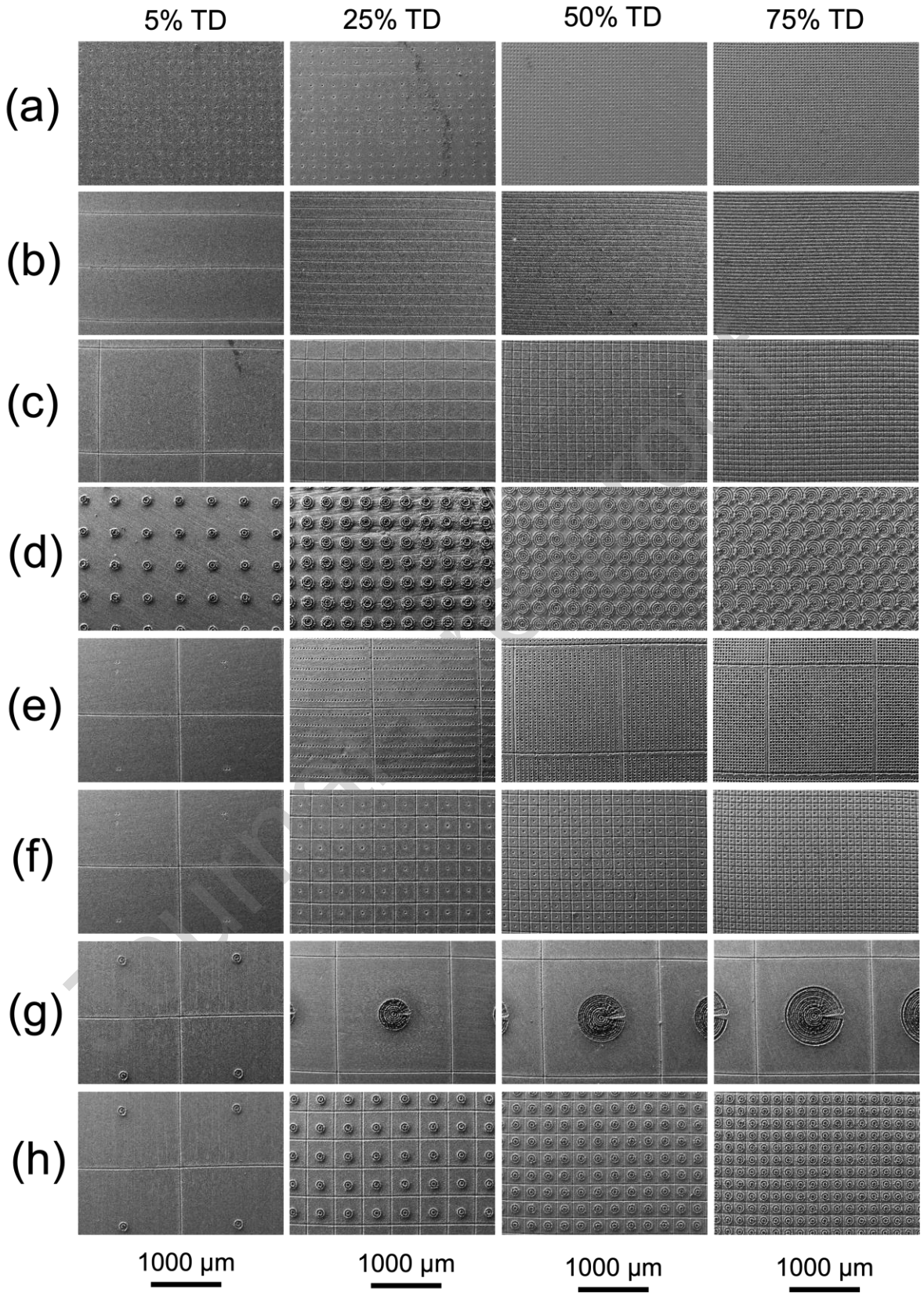

Fig. 5. SEM-SE images of the (a) dimple, (b) groove, (c) grid, (d) concentric ring, (e) dimples-grid, (f) grids-dimple, (g) concentric rings-grid, and (h) grids-concentric ring pattern at 5%, 25%, 50% and, 75% TD on C28000.

Table 4. List of the pattern features according to TD. R_I and R_E correspond to the outermost ring.

Pattern	Features	TD (%)			
		5	**25**	**50**	**75**
Dimple	L_D (μm)	178	80	56	46
Groove	L_G (μm)	840	168	84	56
Grid	L_G (μm)	1659	313	143	84
Concentric ring	L_R (μm)	511	311	324	442
	Ring number	1	2	3	4
	R_I (μm)	30	75	120	179
	R_E (μm)	72	117	162	221
Dimples-grid	L_G (μm)	1678	1678	1678	1678
	L_{DD} (μm)	48	48	48	48
	L_{DL} (μm)	1678	159	71	46
Grids-dimple	L_G (μm)	1667	333	165	109
Concentric rings- grid	L_G (μm)	1805	1805	1805	1805
	Ring number	1	7	11	14
	R_E (μm)	30	324	516	660
	R_I (μm)	72	366	558	702
Grids-concentric ring	L_G (μm)	1805	440	260	191
	R_I (μm)	30	30	30	30
	R_E (μm)	72	72	72	72

3.2. Lubricant service life

Reference tribological tests conducted on non-textured samples (**Fig. 6**) showed that, in the absence of a solid lubricant, the coefficient of friction (COF) rapidly increased to 0.56 ± 0.04 within the first few seconds of operation. This value was adopted as the failure threshold, representing the point at which the MoS_2 coating had fully used its lubricating capacity.

For MoS_2 coated samples, the COF initially increased and then decreased in the first few seconds. The initial increase in friction is attributed to the original topography of the MoS_2 coating. As ball moved over the MoS_2 coating, it polished and compacted the solid lubricant, leading to a reduction in COF [18]. Following the initial reduction, the COF continuously increased over time due to the progressive exfoliation of the MoS_2 coating caused by the ball motion [18]. The COF of the solid lubricant is inversely proportional to its layer thickness [20, 45, 46]. When the COF approached the threshold values of 0.56, it began to fluctuate over time. This phenomenon is attributed to the final layers of the lubricant becoming easily fractured, exposing the sample to direct contact with the counter-body, which increases friction. However, MoS_2 coating remains intact, intermittently reducing the COF [17, 27]. The non-textured samples with MoS_2 coating reached a similar threshold COF (0.56 ± 0.04) after 750 ± 70 s, which was defined as lubricant service life.

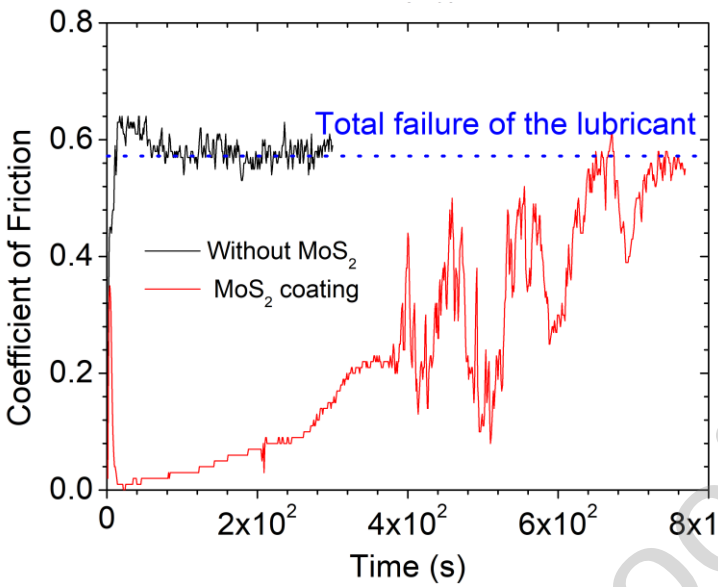

Fig. 6. Temporal evolution of the COF for non-textured samples without and with MoS_2 coating.

All textures patterns exhibited longer lubricant service life compared to non-textured samples (**Fig. 7**). The presence of the textured cavities influenced the tribological process under solid lubrication through two primary effects: lubricant reservoir and debris trapping. The lubricant reservoir effect occurs as MoS_2 accumulates within the textured cavities during deposition. During the tribological testing, the motion and pressure of the counter-body expel the stored lubricant from these cavities, replenishing the MoS_2 lost during testing. This continuous replenishing enhances the lubrication service life [16, 20, 26]. The debris trapping effect occurs as the textured cavities capture the abrasive debris generated during the ball-on-disc testing. These debris contribute to wear and degrade the MoS_2 coating, thereby decreasing the lubricant service life. However, the entrapment of debris within the textured cavities further contributes to extending the lubricant service life [19-21, 25, 26, 47].

The temporal evolution of COF exhibited a consistent pattern across various texture patterns, divided into five stages. In the first stage, the COF behaved similarly to that observed in MoS_2-coated non-textured samples during the initial seconds. Specifically, the COF initially increased before decreasing. The second stage was characterised by a stable COF over time. This stability is attribute to the lubricant reservoir effect of the textured cavities, which helps maintain the integrity of the MoS_2 coating [15, 31]. During the third stage, the COF increased over time, indicating loss of the lubricant reservoir capability of the textures. The accumulation of debris and the loss of the lubricant within texture hindered expulsion of lubricant from cavities [16]. The fourth stage exhibited a fluctuating increase in COF until it reached the threshold value (0.57), signifying the partial removal of the MoS_2 coating. In regions where MoS_2 coating has been removed, direct metal-to-metal contact between the sample and counter-body led to an increase in COF [18, 21, 24]. The observed fluctuations were due to alternating interactions between regions with and without lubricant as the counter-body moved across the sample surface. The reduction in COF during the fluctuation corresponds to regions with MoS_2 coating while the increase in COF associated with the non-lubricated regions [17, 21, 27]. Finally, the fifth stage was characterised by a constant COF value, similar to the previously established threshold value, indicating the total removal of the MoS_2 coating. COF fluctuated over the time due to the generation of the abrasive particles [19] and the topographic changes induced by wear [31]. Notably, the characteristics of C2800, along with the formation

of oxidized particles, contribute to the COF fluctuations observed during the fourth and fifth stages. Harder surfaces, however, reduce these fluctuations, as indicated in previous studies [48, 49].

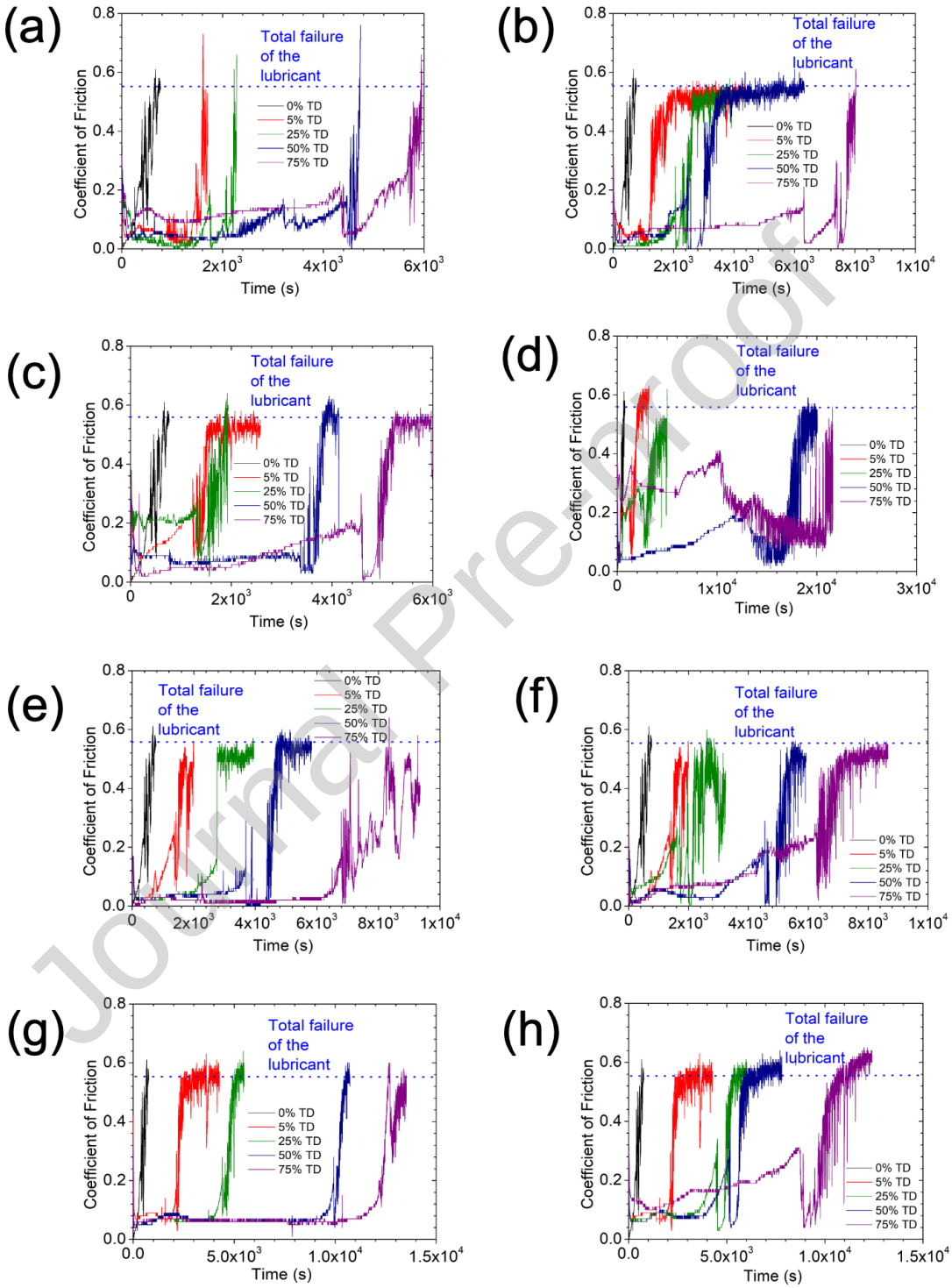

Fig. 7. Temporal evolution of the COF (a) dimple, (b) groove, (c) grid, (d) concentric ring, (e) dimples-grid, (f) grids-dimple, (g) concentric rings-grid and (h) grids-concentric ring pattern with MoS_2 coating.

Fig. 8. illustrates the lubricant service time of various texture patterns as a function of TD. An increase in TD extended the lubricant service life across all texture patterns, primarily due to

the increased lubrication reservoir capacity and the enhanced debris-trapping effect. The amount of the lubrication reservoir is directly proportional to the number of texture features, while the duration of the reservoir effect is, in turn, proportional to the quantity of lubricant retained [21, 26]. A higher number of the texture cavities enhances both the quantity captured debris and the likelihood of effective debris entrapment [18, 19, 21]. The non-texture regions exhibit a thinner MoS_2 coating compared to the textured regions. The lubricant failure occurs more readily in areas with a thinner MoS_2 coating. Therefore, reducing the proportion of regions with thin MoS_2 coating decreases the likelihood of lubricant failure, thereby extending the lubricant service life [18, 21]. The patterns featuring concentric rings (i.e., concentric rings, concentric rings-grid, and grids-concentric ring patterns) exhibited the longest lubricant service time, with a significant improvement compared to other type of texture patterns. The shape of the pattern influences on the dynamic pressure by the counter-body on the lubricated surface [35-39], which in turn define the expelling rate of the reserved lubricant [35]. The specific concentric rings shape appears to exhibit the optimal dynamic pressure effect for the solid lubrication due to its synodic morphology [38]. Among the patterns containing concentric rings, the surfaces textured exclusively with concentric rings presented the longest lubricant service life, whereas the grid-concentric ring pattern exhibited the shortest lubricant service life for the same TD. This result is attributed to the presence of the grid features within the pattern, which can disrupt the dynamic pressures characteristics observed in the concentric rings. This assertion is further examined in Section 3.3 using finite element analysis simulation. The ring textures exhibit superior dynamic pressure compared to the classic groove or grids [50]. The dynamic pressure effect of the concentric ring can also amplify by increasing in the concentric ring number, as indicated by the longer lubrication service life of the concentric rings-grid patterns compared to grid-concentric ring pattern.

Among the remained patterns (dimple, groove, grid, dimples-grid, and grids-dimple patterns), the groove patterns exhibited the longest lubricant service life, while the grid patterns presented the shortest. This result confirms the importance of the texture pattern morphology in determining lubrication performance. The dimple, dimples-grid, and grids-dimple patterns exhibited similar lubricant service life, indicating that dimples have a more significant impact in compared to the grid textures. Comparable findings were reported by Zhan et al [51] for dimple-groove patterns under oil lubrication conditions. It is important to highlight that the grid patterns demonstrated the shortest lubricant service life, suggesting that these influence on the lubricant performance is lower than that of other types of textures. This assertion is further studied in Section 3.3 throughout finite element analysis simulation. The grid texture pattern demonstrates a more homogenous spatial distribution of the pressure or stress compared to the dimple and groove patterns [52]. This uniform stress can decrease the solid lubricant ejection form the textured cavities, resulting in the reduction of the lubricant service life.

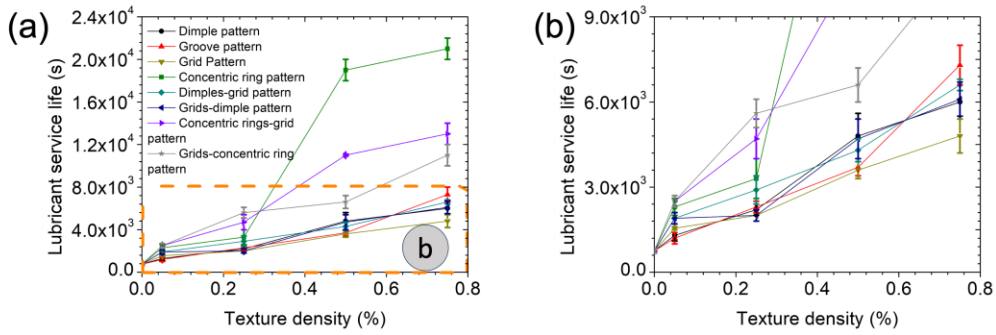

Fig. 8. Lubricant service life of the texture patterns as a function of texture density. The initial area is magnified and redrawn in graph (b) for clarity.

3.3. Finite element analysis of the hybrid texture patterns.

Fig. 9 shows the spatial distribution of normal stresses for the dimple (**Fig. 9(a)**), grid (**Fig. 9(b)**), concentric ring (**Fig. 9(c)),** dimples-grid (**Fig. 9(d))**, grids-dimple (**Fig. 9(e)**), concentric rings-grid (**Fig. 9(f)**), and grids-concentric ring (**Fig. 9(g)**) patterns obtained from finite element simulations. Stress is represented in greyscale: black tones indicate positive stresses (opposite to the applied load), while white tones represent negative stresses (in the same direction as the applied load).

Across most patterns, maximum negative stresses were concentrated at the centre of the ball–sample contact, typically surrounded fully or partially by regions of positive stress. Positive stresses favour lubricant ejection from cavities, whereas negative stresses promote MoS_2 compression within cavities. This spatial stress distribution governs the rate of lubricant replenishment from textured reservoirs to the surface [35].

The grid, concentric rings-grid, and grids-concentric ring textures showed minimal or negligible regions of positive stress. In these cases, the weak positive stresses could not counterbalance the strong negative stresses, reducing the ability of lubricant to be expelled. As a result, part of the stored MoS_2 remained trapped in cavities until the coating failed.

Fig. 10 summarises the maximum positive and negative stresses across all textures. In absolute terms, maximum negative stresses consistently exceeded positive stresses, confirming that compression of the lubricant dominates across all designs. The magnitudes were strongly dependent on texture morphology. Hybrid textures, particularly those containing concentric rings, exhibited the largest stress magnitudes and the widest disparity between negative and positive stresses. These imbalances reduce the rate of lubricant release, further shortening MoS_2 service life.

Therefore, the inferior performance of hybrid concentric ring patterns compared to simple concentric rings can be attributed to stress distortion and amplification introduced by the grid component. The combined geometry disrupts favourable stress distributions, increases stress asymmetry, and ultimately hinders lubricant replenishment.

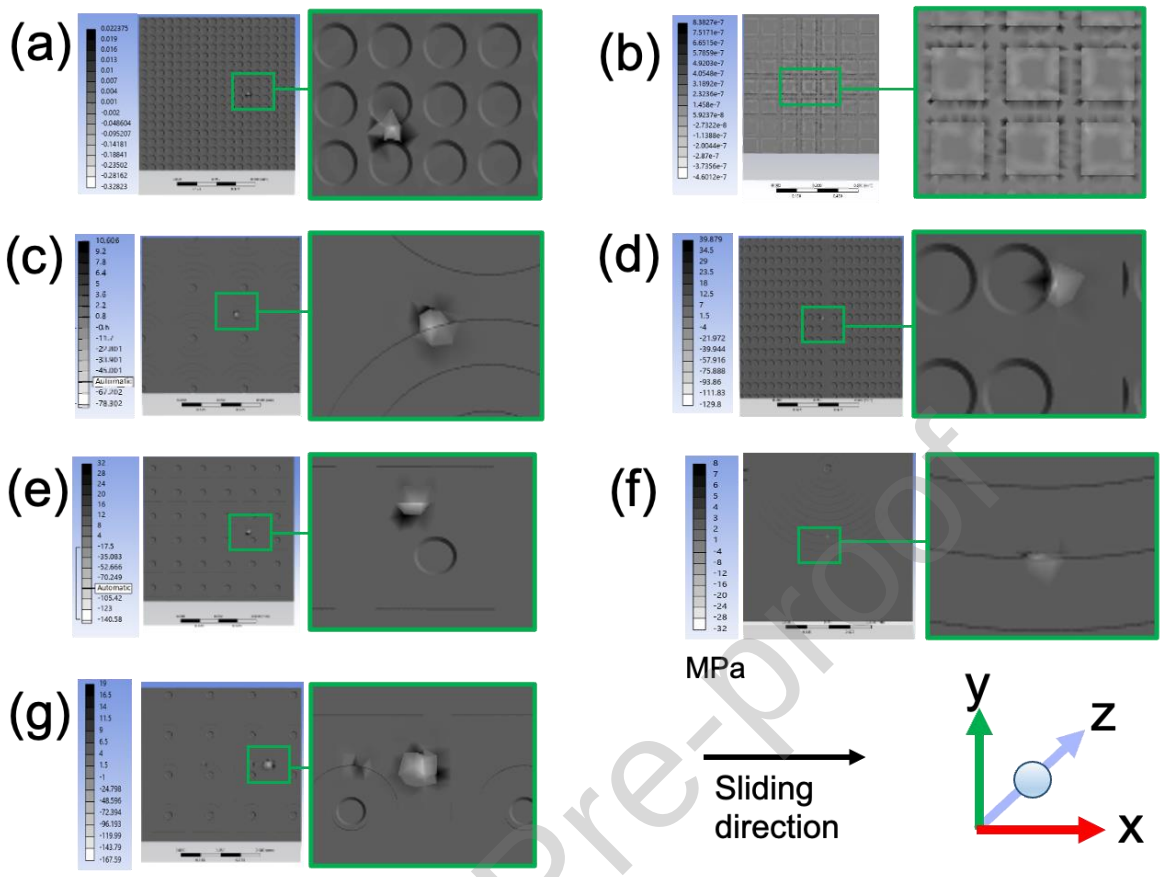

Fig. 9. Finite element simulation results showing normal stress distribution for (a) dimples, (b) grid, (c) concentric ring, (d) dimples-grid, (e) grids-dimple, (f) concentric rings-grid, and (g) grids-concentric ring patterns.

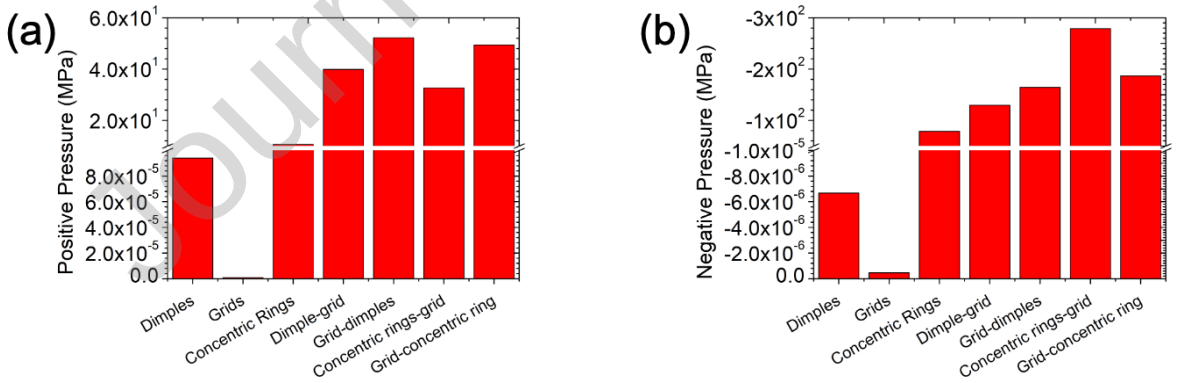

Fig. 10. Maximum (a) positive and (b) negative surface stresses for dimple, grid, concentric ring, dimples-grid, grids-dimple, concentric rings-grid, and grids-concentric ring patterns.

3.4. Assessment of the morphology temporal evolution during ball-on-disc

Fig. 11 illustrates the evolution of the worn track and ball (counter-body) over time, which was the same across all patterns. The progression of the wear on both worn track and ball followed five stages, corresponding to the COF stage observed over time.

In the first stage, the worn track exhibited distinct three regions with different characteristics: the edges, laterals, and centre of the worn track. This heterogeneous morphology is attributed non-uniform pressure distribution exerted by the ball. Due to the spherical shape of the ball, the maximum pressure is concentrated at the centre of the contact area, gradually decreasing toward the edges [37]. At the edges of the worn track, the accumulation of the MoS_2 was observed, forming a smooth surface. This phenomenon occurs due to heterogeneous pressure distribution, which causes the ejection from the centre of the contact area toward the edges, where the low pressure of the ball allows its accumulation. This displacement of the solid lubricant also accounts for the lower MoS_2 concentration in the centre and lateral of the worn track compared to the regions outside track. The relative motion of the ball over the MoS_2 accumulated at the edges also polishes the solid lubricant surface [29]. The lateral of the worn tracks exhibited MoS_2 accumulations within the texture cavities, as well as conglomerations of the solid lubricant particles. The presence of the solid lubricant within the textures confirms their function as lubricant reservoir [16, 19, 21]. The formation of the conglomerations is attributed to expulsion of the solid lubricant form texture, however, the expelled lubricant is insufficient to form a MoS_2 coating [15, 21]. The lubrication ejection rate is proportional to the pressure, which remains low in this contact area region [15, 21]. In contrast, a homogeneous MoS_2 layer was observed in the centre of the worn track. The high-pressure facilities an optimal lubrication ejection rate, leading to the formation of a uniform MoS_2 layer [15, 21, 31]. At this stage, the solid lubricant was absent on the ball surface, indicating the minimum adhesion of the MoS_2 to counter-body surface.

At the second stage, the worn track exhibited a morphology similar to that observed in the previous stage. However, the overall size of the worn track increased compared to earlier stage, indicating the progressive wear of the MoS_2 coating. The wear of the ball on the MoS_2 coating intensified with the increase in test duration [21]. The MoS_2 layer at the centre of the worn track also became heterogeneous. The solid lubricant in the worn track centre is gradually expelled from the centre toward edges, leading to reduction in the MoS_2 concentration at centre. This expulsion of the lubricant reserve occurred around the texture features [15, 26, 31], contributing to the heterogeneity of the layer. The ball surface exhibited agglomerations of the MoS_2 coating. A portion of the kinetic energy is converted to the heat due to the friction effect, leading to increase in the temperature of both ball and the solid lubricant. The temperature rise is directly proportional to test duration, as prolonged friction continuously transforms kinetic energy into heat [19, 25, 27]. The elevated temperature facilities the adhesion of the MoS_2 onto the ball surface [25].

In the third stage, the worn track continued to expand, and its edges was devoid of MoS_2 accumulation. The continuous polishing effect of the ball on the solid lubricant previously accumulated along the worn track led to in this region. Other characteristics of the worn track remained with those observed in previous stages. The ball exhibited a smooth and heterogeneous MoS_2 coating, indicating increased adhesion of the solid lubricant to the counter-body. The growing concentration of the MoS_2 on the ball contributed to layer formation, which is subsequently polished due the relative motion between the ball and the sample [17].

At the fourth stage, the direct contact between the sample and counter-body was observed, as indicated by the characteristic of both the worn track and the ball. The worn track exhibited a homogeneous surface with the presence of scratches, cracks, and adhered particles. The formation of the scratches is attributed to the generation of the abrasive particles, which impact the surfaces during testing [21, 27, 28]. The crack formation is due to fatigue mechanisms cause

by the relative motion of the ball on the sample surface and the pressure exerted by the counter-body [16]. Regarding particle adhesion, debris generated during the testing is adhered on the ball in specific regions. As the counter-body moved, debris adhered on the ball can detach onto different zones of the sample. Subsequently, during repeated passes of the ball, the deposited debris becomes compacted into the surface, increasing adhesion [17, 27, 28, 53]. The presence of the sample particles on the ball surface indicated the adhesion of the C28000 on the counter-body at this stage. The worn track also exhibited some regions where the part of the MoS_2 remained within the texture. This residual lubricant continued to contribute to lubrication during the tribological test, which explains the low COF compared to the COF under dry condition (0.57). The presence of MoS_2 on the ball surface confirmed that a portion of the lubricant remained active in this stage.

In the final stage, both the worn track and the ball exhibited an almost complete absence of lubricant, indicating the total failure of the MoS_2 as an effective lubricant. The ball surface also displayed transferred material from the sample, suggesting that the dragging process persisted during this stage. Apart from the absence of solid lubricant, the overall appearance of the worn track was similar than that observed in the previous stage.

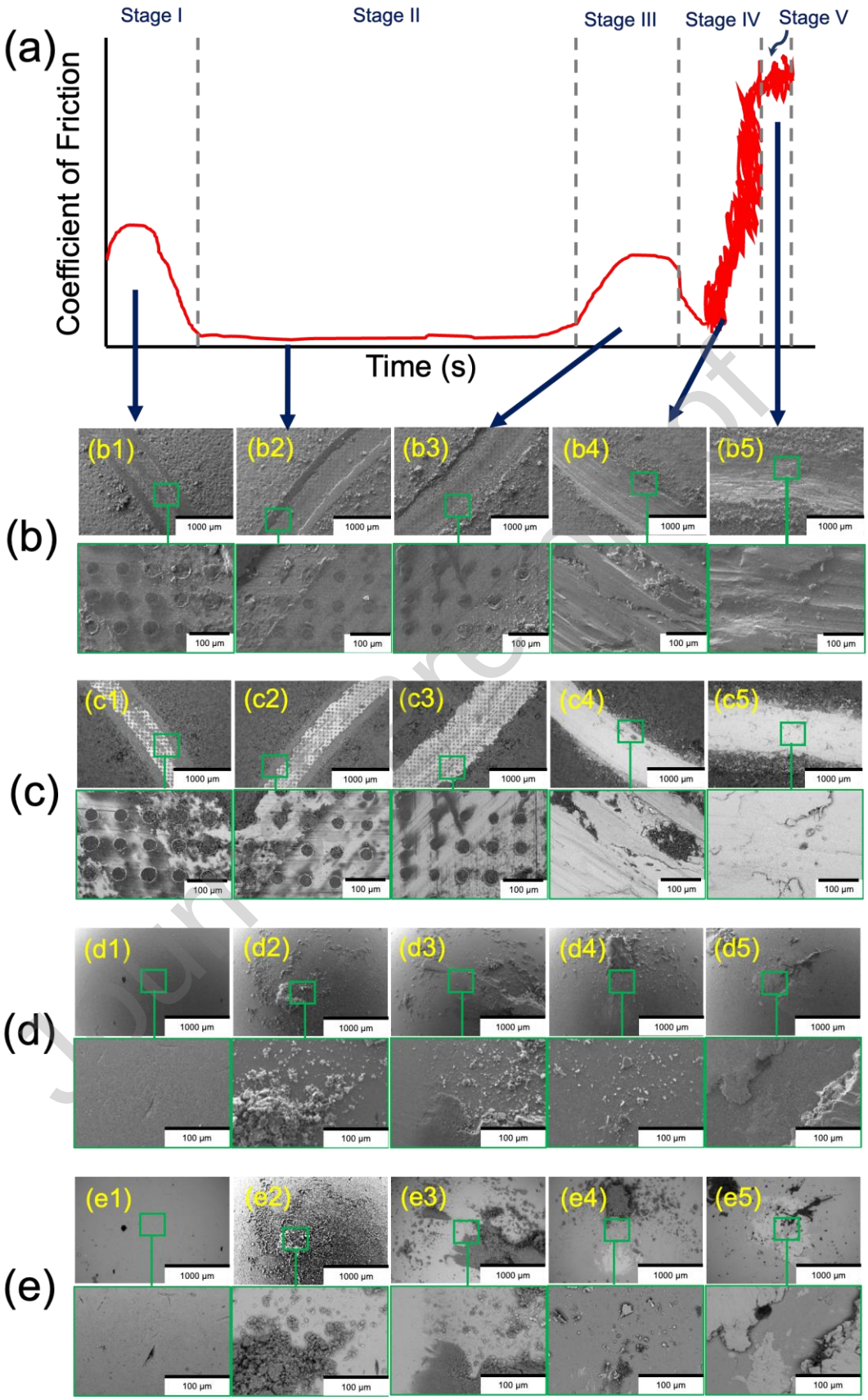

Fig. 11. (a) Schematic drawing of the temporal evolution of COF for the textured surface. (b-e) SEM-(b, d) SE and – (c,e) BSE of the (b-c) worn track and (d-c) counter-body for dimple pattern at 25% TD according to the stage.

The samples exhibited the presence of molybdenum, sulphur, oxygen, carbon, copper, and zinc across all stages, whereas the chemical composition of the ball surface varied throughout the different stages (**Fig. 12**). Molybdenum and sulphur on the sample surface corresponded to MoS_2, while copper and zinc associated with C2800 alloy. Oxygen and carbon, although potentially originating from the contamination, were found in lower concentrations within the worn track compared to other regions of the sample. This observation suggests that these elements associated with the MoS_2 coating. Organic compounds are commonly employed to improve the adhesion MoS_2 to the substrate and to reduce curing time [54]. Although the presence of these elements remained across different stages, their distribution changed. Despite the chemical composition of the ball varied for each stage, iron and chromium were consistently detected. 52100 steel used for the ball is primarily composed of iron and chromium [55]. At the first stage (**Fig. 12(a)**), the elements associated with the solid lubricant within the worn track exhibited lower concentration compared to other localisations of the sample. The motion of the ball across the surface rapidly removes the external MoS_2 layer due to low adhesion to the substrate [21, 27]. Notably, the textured regions presented the highest concentration of the lubricant within the track, validating its function as lubricant reservoir. The low concentration of the solid lubricant elements were also observed on the ball surface, indicating the initial adhesion of the MoS_2 to the counter-body.

In the second (**Fig. 12(b)**) and third (**Fig. 12(c)**) stages, the worn track exhibited similar appearance to that observed in the previous stage. However, the ball surface in the second stage (**Fig. 12(b)**) showed a considerable increase in the MoS_2 coating-related elements, suggesting the accumulation of the solid lubricant on the counter-body. In the third stage (**Fig. 12(c)**), copper and zinc were detected on the ball surface in association with MoS_2. Despite this, the sample surface remained intact within the worn track at this stage. The presence of the C2800 alloy debris is likely due to the micro-fracturing of the texture crest. Due to their reduced contact area, these crests experience high pressures from the ball [16]. It is important to note that the small size of the debris contributes to their integration within the solid lubricant [16, 19]. The formation and accumulation of debris typically induce a rapid rise and pronounced fluctuations in COF for harder materials [49, 56]. In the present case, however, only a modest COF with negligible fluctuations was observed, which can be attributed to the generation of comparatively softer debris.

The worn track contained some MoS_2 particles at the fourth stage (**Fig. 12(d)**), whereas in the fifth stage (**Fig. 12(e)**), the worn track was devoid of the solid lubricant. This observation suggests that while the lubricant remained in worn track at the fourth stage, whereas it was entirely depleted at fifth stage. In the case of the ball, the amount of the solid lubricant reduced from fourth stage to fifth stage, while the presence of the C2800 particles were increased. This trend indicates a progressive process of wear in the sample for both stages. It is important to note that the concentration of oxygen was lower in the track in comparison with other regions of the sample. This observation suggests the absence of the C2800 oxidation and, consequently, the lack of the abrasive oxidised particles formation.

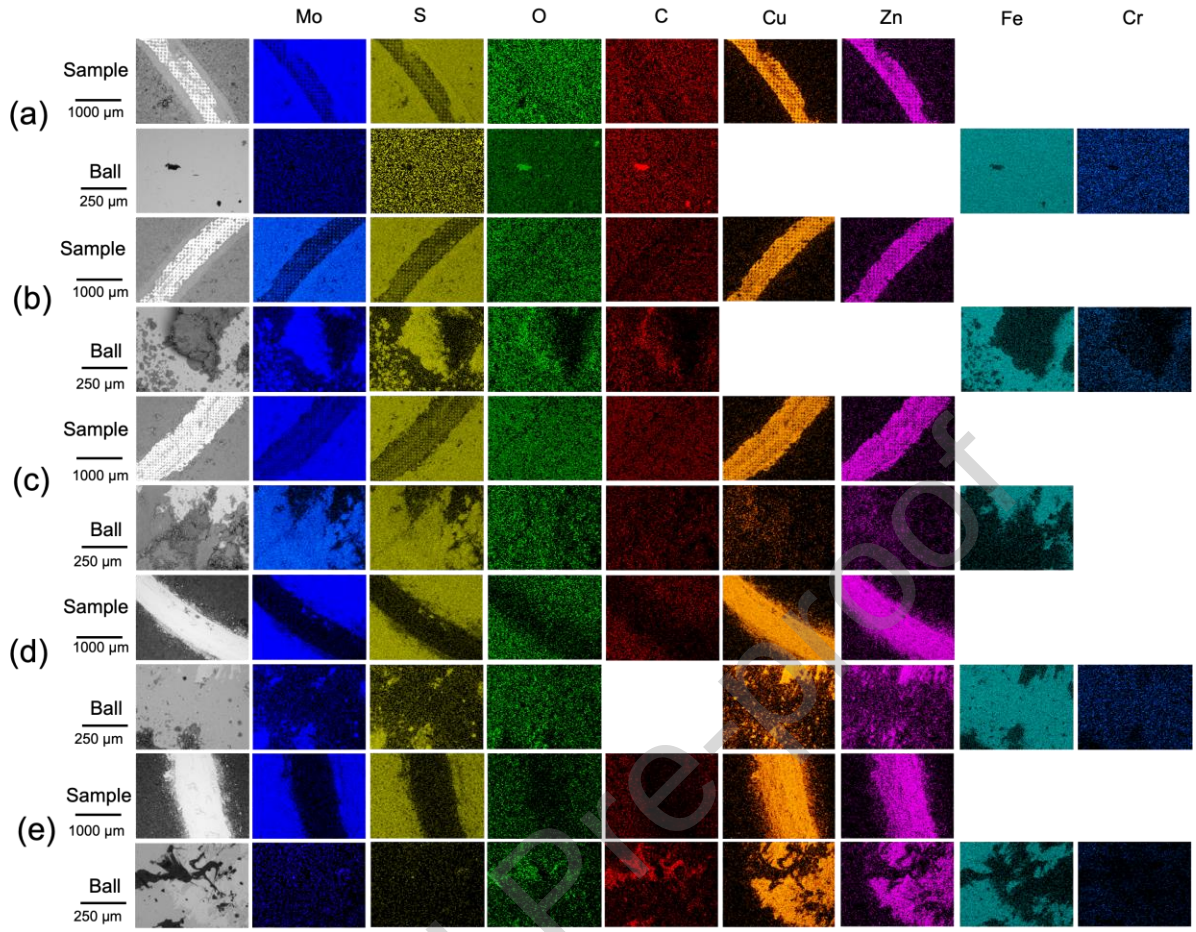

Fig. 12. EDS mapping of both worn track and ball for (a) first, (b) second, (c) third, (d) fourth, and fifth stages for the dimple pattern of 25% TD.

In the centre of the worn track, the concentration of the molybdenum and sulphur was reduced with each successive stage, while those of the copper and zinc increased (**Fig. 13**). This trend indicates a progressive depletion of the lubricant over the testing duration. Conversely, the concentration of molybdenum and sulphur increased at the edges of the worn track as the test progressed. The heterogeneous pressure distribution within the contact area drives the ejection of the lubricant from the high-pressure regions toward low-pressure zones [15, 21]. This outward expulsion of the solid lubricant is likely the primary factor contributing to the failure of the lubricant coating.

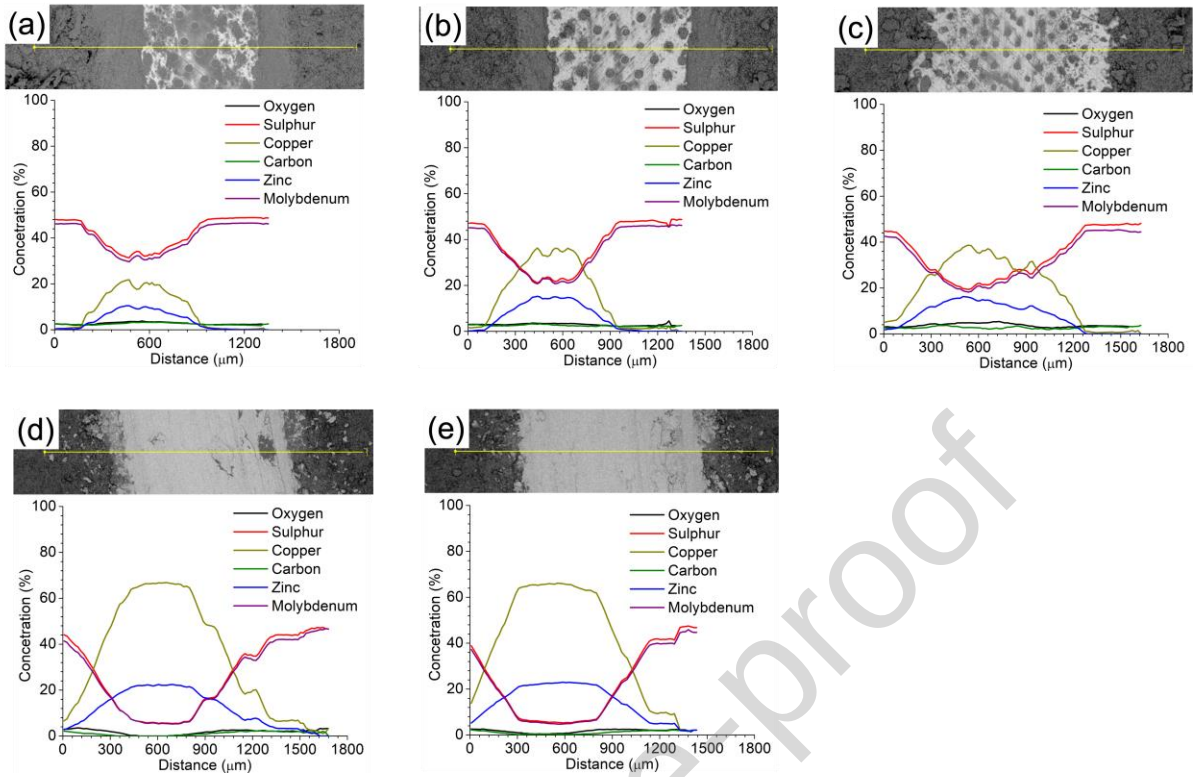

Fig. 13. EDS of the worn track in the (a) first, (b) second, (c) third, (d) fourth, and (e) fifth stages for the dimple pattern of 25% TD.

4. Conclusions

This study examined the effects of the LST and the texture pattern parameters (TD and shape) on the tribological properties of the MoS_2 coated C28000. The investigation provided significant insights into the lubrication service life, temporal evolution of the coating, and the mechanisms underlying lubricant failure, including less-common patterns as concentric ring pattern. The key findings are outlined below:

1. LST improves the lubricant service life of MoS_2 due to three key functions of the textured cavities: serving as a lubricant reservoir, acting as a debris trap, and promoting the thickening of the lubricant coating.
2. An increase in TD enhances the lubricant service life across all textures patterns by improving the effectiveness of the texture key functions.
3. The morphology of the texture patterns plays a crucial role in determining the lubricant service life, as it directly influences the rate at which the lubricant reservoir is ejected. The concentric ring pattern was found to be the most effective for maximising lubricant service life, whereas the grid pattern showed the least beneficial effect.
4. The temporal evolution of the coefficient of friction for the concentric ring pattern exhibited comparable behaviour to other texture pattern (five stages), but with markedly more extended lubrication service life.
5. The combination of different texture types provides minimal benefit, and in some cases, significantly reduces the performance of the patterns based on concentric ring textures (e.g., concentric rings-grid and grids-concentric ring pattern).
6. The failure of the MoS_2 coating occurs due to the thinning of the layer, which results from the expulsion of the solid lubricant from the centre of the worn track to the outer

regions. This expulsion is driven by the heterogeneous pressure distribution within the contact area.

The results of this study are essential for designing surfaces that enhance lubricant service life, which is critical across various industries. Applications include automotive components such as pistons, bearings, and bushings; energy systems like piston coatings; aerospace components including wheel bearings, landing gear bearings, and bushings; maritime bearings; offshore wind turbines, such as coil bearings; and construction bushings. In future studies, the effects of temperature, high-load contact, and aggressive environments on the tribological behaviour of laser-textured C2800 will be investigated to assess performance under representative industrial conditions. This research provides valuable insights into the tribological behaviour of MoS_2-coated texture patterns, advancing the understanding of their wear and lubrication mechanisms in relation to surface morphology.

STATEMENTS AND DECLARATIONS

Funding

The authors acknowledge Liverpool John Moores University (LJMU) for institutional support. No external funds, grants, or other financial support were received during the preparation of this manuscript.

Conflicts of interest

There are no conflicts of interest.

Author Contributions

Juan Ignacio Ahuir-Torres contributed to the conception and design of the study. Material preparation, data collection, the first draft of the manuscript, the analysis and discussion of the results were carried out by Juan Ignacio Ahuir-Torres. Sian Evans contributed to the data acquisition. All authors provided feedback and contributed to the development of subsequent versions of the manuscript. All authors have read and approved the final manuscript.

Data Availability Statement

The datasets generated during and/or analysed during the current study are available in the manuscript

References

[1] Liu Z, Messer-Hannemann P, Laube S, Greiner C. Tribological performance and microstructural evolution of α-brass alloys as a function of zinc concentration. Friction. 2020;8:1117-36.
[2] Sun Y, Xu N, Fujii H. The microstructure and mechanical properties of friction stir welded Cu–30Zn brass alloys. Mater Sci Eng A. 2014;589:228-34.
[3] Kaiser S, Kaiser M. Wear behavior of commercial pure copper with Al and Zn under dry, wet and corrosive environment. J Mater Environ Sci. 2020;11:551-63.
[4] ketika Proses PWT. PISTON. J TechnEng Piston Vol. 2020;4:1-10.
[5] Epshteyn Y, Risdon T. Molybdenum disulfide in lubricant applications–A review.[Paper presentation]. Proceedings of the 12 Lubricating Grease Conference, Goa, India http://www nlgi-india org/images/PDF/Yakov% 20Ephsteyn pdf2010.

[6] Vazirisereshk MR, Martini A, Strubbe DA, Baykara MZ. Solid lubrication with MoS2: a review. Lubr. 2019;7:57.
[7] Gajrani KK, Sankar MR, Dixit US. Environmentally friendly machining with MoS 2-filled mechanically microtextured cutting tools. J Mech Sci Technol. 2018;32:3797-805.
[8] Xu Y, Yu J, Geng J, Abuflaha R, Olson D, Hu X, et al. Characterization of the tribological behavior of the textured steel surfaces fabricated by photolithographic etching. Tribol Lett. 2018;66:1-15.
[9] Hudson WR. Ion beam texturing. Vacuum Symp1976.
[10] Shamsul Baharin AF, Ghazali MJ, A Wahab J. Laser surface texturing and its contribution to friction and wear reduction: a brief review. Ind Lubr Tribol. 2016;68:57-66.
[11] Nsilani Kouediatouka A, Ma Q, Liu Q, Mawignon FJ, Rafique F, Dong G. Design methodology and application of surface texture: A review. Coat. 2022;12:1015.
[12] Rodrigues T, Arencibia R, Costa H, Da Silva W. Roughness analysis of electrochemically textured surfaces: effects on friction and wear of lubricated contacts. Surf Topogr Metrol Prop. 2020;8:024011.
[13] Zhou R, Cao J, Wang QJ, Meng F, Zimowski K, Xia ZC. Effect of EDT surface texturing on tribological behavior of aluminum sheet. J Mater Process Technol. 2011;211:1643-9.
[14] Huang Q, Shi X, Xue Y, Zhang K, Wu C. Recent progress on surface texturing and solid lubricants in tribology: Designs, properties, and mechanisms. Mater Today Commun. 2023;35:105854.
[15] Xie X, Hua X, Li J, Cao X, Tian Z, Peng R, et al. Synergistic effect of micro-textures and MoS2 on the tribological properties of PTFE film against GCr15 bearing steel. J Mech Sci Technol. 2021;35:2151-60.
[16] Hua X, Xie X, Yin B, Zhang P, Ji J, Wang H, et al. Tribological performance and self-lubricating mechanism of the laser-textured surface filled with solid lubricant in rolling friction pair. Ind Lubr Tribol. 2018;70:371-84.
[17] Feng X, Wang R, Wei G, Zheng Y, Hu H, Yang L, et al. Effect of a micro-textured surface with deposited MoS2-Ti film on long-term wear performance in vacuum. Surf Coat Technol. 2022;445:128722.
[18] Qin Y, Xiong D, Li J. Tribological properties of laser surface textured and plasma electrolytic oxidation duplex-treated Ti6Al4V alloy deposited with MoS2 film. Surf Coat Technol. 2015;269:266-72.
[19] Ripoll MR, Simič R, Brenner J, Podgornik B. Friction and lifetime of laser surface–textured and MoS 2-Coated Ti6Al4V under dry reciprocating sliding. Tribol Lett. 2013;51:261-71.
[20] Arenas M, Ahuir-Torres JI, García I, Carvajal H, De Damborenea J. Tribological behaviour of laser textured Ti6Al4V alloy coated with MoS2 and graphene. Tribol Int. 2018;128:240-7.
[21] Hu T, Hu L. Tribological properties of lubricating films on the Al-Si alloy surface via laser surface texturing. Tribo T. 2011;54:800-5.
[22] Mao B, Siddaiah A, Liao Y, Menezes PL. Laser surface texturing and related techniques for enhancing tribological performance of engineering materials: A review. Journal of Manufacturing Processes. 2020;53:153-73.
[23] Li J, Xiong D, Wu H, Zhang Y, Qin Y. Tribological properties of laser surface texturing and molybdenizing duplex-treated stainless steel at elevated temperatures. Surf Coat Technol. 2013;228:S219-S23.
[24] Hu T, Zhang Y, Hu L. Tribological investigation of MoS2 coatings deposited on the laser textured surface. Wear. 2012;278:77-82.
[25] Voevodin A, Zabinski J. Laser surface texturing for adaptive solid lubrication. Wear. 2006;261:1285-92.

[26] Rapoport L, Moshkovich A, Perfilyev V, Lapsker I, Halperin G, Itovich Y, et al. Friction and wear of MoS2 films on laser textured steel surfaces. Surf Coat Technol. 2008;202:3332-40.
[27] Zhang K, Deng J, Lei S, Yu X. Effect of micro/nano-textures and burnished MoS2 addition on the tribological properties of PVD TiAlN coatings against AISI 316 stainless steel. Surf Coat Technol. 2016;291:382-95.
[28] Xing Y, Deng J, Wang X, Meng R. Effect of laser surface textures combined with multi-solid lubricant coatings on the tribological properties of Al2O3/TiC ceramic. Wear. 2015;342:1-12.
[29] Xing Y, Deng J, Wu Z, Cheng H. Effect of regular surface textures generated by laser on tribological behavior of Si3N4/TiC ceramic. Appl Surf Sci. 2013;265:823-32.
[30] Bagade VU, Duraiselvam M, Sarangi N, Parthiban K. Effect of laser surface texturing on coating adherence and tribological properties of CuNiIn and MoS 2 coating. Transactions of the Indian Institute of Metals. 2022:1-12.
[31] Segu DZ, Kim J-H, Choi SG, Jung Y-S, Kim S-S. Application of Taguchi techniques to study friction and wear properties of MoS2 coatings deposited on laser textured surface. Surf Coat Technol. 2013;232:504-14.
[32] Al-Mahdy A, Kotadia H, Sharp M, Opoz T, Mullett J, Ahuir-Torres J. Effect of surface roughness on the surface texturing of 316 l stainless steel by nanosecond pulsed laser. Lasers in Manufacturing and Materials Processing. 2023;10:141-64.
[33] Schneider J, Braun D, Greiner C. Laser textured surfaces for mixed lubrication: influence of aspect ratio, textured area and dimple arrangement. Lubr. 2017;5:32.
[34] Gachot C, Rosenkranz A, Hsu S, Costa H. A critical assessment of surface texturing for friction and wear improvement. Wear. 2017;372:21-41.
[35] Xu Z, Zhang Q, Huang X, Zhai W, Yang K, Zhu Q. An approximate model for the migration of solid lubricant on metal matrix self-lubricating composites. Tribol Int. 2016;93:104-14.
[36] Hu T, Xie L, Chen J, Huang Z, Wang J. Numerical study on tribology properties of textured surfaces based on a new contact model. Mater Today Commun. 2024;40:109969.
[37] Zhang J, Yang D, Rosenkranz A, Zhang J, Zhao L, Song C, et al. Laser surface texturing of stainless steel− effect of pulse duration on texture's morphology and frictional response. Advanced Engineering Materials. 2019;21:1801016.
[38] Ma J, Liu Y, Yi P, Jia H, Zhang N, Sun J. Anti-friction mechanism of sinusoidal texture with various intervals: The synergistic effect of dynamic pressure and tribofilm. Tribol Int. 2022;173:107635.
[39] Yu H, Wang X, Zhou F. Geometric shape effects of surface texture on the generation of hydrodynamic pressure between conformal contacting surfaces. Tribol Lett. 2010;37:123-30.
[40] Gropper D, Wang L, Harvey TJ. Hydrodynamic lubrication of textured surfaces: A review of modeling techniques and key findings. Tribol Int. 2016;94:509-29.
[41] Holder D, Weber R, Graf T. Analytical model for the depth progress during laser micromachining of V-shaped grooves. Micromachines. 2022;13:870.
[42] Fishburn J, Withford M, Coutts D, Piper J. Study of the fluence dependent interplay between laser induced material removal mechanisms in metals: Vaporization, melt displacement and melt ejection. Appl Surf Sci. 2006;252:5182-8.
[43] Zhu Y, Fu J, Zheng C, Ji Z. Effect of nanosecond pulse laser ablation on the surface morphology of Zr-based metallic glass. Opt Laser Technol. 2016;83:21-7.
[44] Bulgakova N, Bulgakov A. Pulsed laser ablation of solids: transition from normal vaporization to phase explosion. Appl Phys A. 2001;73:199-208.
[45] Tang G, Zhang J, Liu C, Zhang D, Wang Y, Tang H, et al. Synthesis and tribological properties of flower-like MoS2 microspheres. Ceramics International. 2014;40:11575-80.

[46] Erdemir A. Solid lubricants and self-lubricating films. Modern tribology handbook. 2001;2:787-818.
[47] Wu S, Wang Y, Jiang X, Hu S, Yao C, Dong B, et al. Bioinspired femtosecond laser surface texturing for enhancing tribological properties of Ti6Al4V titanium alloy. Tribol Int. 2025:110987.
[48] Yuan S, Lin N, Wang W, Zhang H, Liu Z, Yu Y, et al. Correlation between surface textural parameter and tribological behaviour of four metal materials with laser surface texturing (LST). Appl Surf Sci. 2022;583:152410.
[49] Yuan S, Lin N, Zou J, Liu Z, Wang Z, Tian L, et al. Effect of laser surface texturing (LST) on tribological behavior of double glow plasma surface zirconizing coating on Ti6Al4V alloy. Surf Coat Technol. 2019;368:97-109.
[50] Wang H, Zhu H, Zhou Y, Yang H. Experimental study on the friction characteristics of textured steel surface with ring-shaped pits under lubricated sliding conditions. Tribology Transactions. 2015;58:712-7.
[51] Zhan X, Yi P, Liu Y, Xiao P, Zhu X, Ma J. Effects of single-and multi-shape laser-textured surfaces on tribological properties under dry friction. Proceedings of the Institution of Mechanical Engineers, Part C: Journal of Mechanical Engineering Science. 2020;234:1382-92.
[52] Lu L, Zhang Z, Guan Y, Zheng H. Comparison of the effect of typical patterns on friction and wear properties of chromium alloy prepared by laser surface texturing. Optics & Laser Technology. 2018;106:272-9.
[53] Zhang X, Jiang J, Li S, Wen D. Laser textured Ti-6Al-4V surfaces and grinding performance evaluation using CBN grinding wheels. Opt Laser Technol. 2019;109:389-400.
[54] Tonge P, Roy A, Patel P, Beall CJ, Stoyanov P. Environmentally friendly bonded MoS2 solid film lubricants for aerospace applications: closing the gap. Sustainable Materials and Technologies. 2023;35:e00552.
[55] Guo Y, Liu C. Mechanical properties of hardened AISI 52100 steel in hard machining processes. J Manuf Sci Eng. 2002;124:1-9.
[56] Lei X, Lin N, Yuan S, Lei C, Nouri M, Liu Z, et al. Combining laser surface texturing and double glow plasma surface chromizing to improve tribological performance of Ti6Al4V alloy. Surf Coat Technol. 2024;478:130418.

Declaration of Competing Interest

The authors declare that they have no known competing financial interests or personal relationships that could have appeared to influence the work reported in this paper.

Statement of Originality

The authors confirm that this manuscript is an original work and has not been published previously in any form or language, nor is it under consideration for publication elsewhere. All data, analyses, and interpretations presented are the authors' own, and where the work of others has been used, it has been appropriately cited and referenced. The study has been conducted in accordance with ethical publishing practices, and the authors declare no conflicts of interest.